NUCL SCI TECH (2016) 27:66
DOI 10.1007/s41365-016-0071-0

3D microstructures of nuclear graphite: IG-110, NBG-18 and NG-CT-10

Shi-Pei Jing[1,2] · Can Zhang[2] · Jie Pu[2] · Hong-Yan Jiang[2] · Hui-Hao Xia[2] · Fang Wang[1] · Xu Wang[1] · Jian-Qiang Wang[2] · Chan Jin[2]

Received: 3 June 2015 / Revised: 8 October 2015 / Accepted: 8 October 2015 / Published online: 11 May 2016

Abstract Molten salt is used as primary coolant flowing through graphite moderator channel of a molten salt reactor. Working at high temperature under radiation environment, the pore network structure of nuclear graphite should be well understood. In this paper, X-ray tomography is employed to study the 3D pore structure characteristics of nuclear grades graphite of IG-110, NBG-18 and NG-CT-10, and permeability simulation through geometries are performed. The porosity, number of pores and throats, coordination number and pore surface are obtained. NG-CT-10 is of similar microstructure to IG-110, but differs significantly from NBG-18. The absolute permeabilities of IG-110, NG-CT-10 and NBG-18 are 0.064, 0.090 and 0.106 mD, respectively. This study provides basis for future research on graphite infiltration experiment.

Keywords X-ray tomography · 3D pore network structure · Permeability

This work was supported by National Natural Science Foundation of China (Nos. 11275256 and 11179024), and Program of International S&T Cooperation (No. 2014DFG60230).

✉ Chan Jin
jinchan@sinap.ac.cn

1 College of Physics and Electronic Engineering, Henan Normal University, Xinxiang, Henan 453007, China

2 Shanghai Institute of Applied Physics, Chinese Academy of Sciences, Jiading Campus, 2019 Jia Luo Road, Jiading District, Shanghai 201800, China

1 Introduction

Molten salt reactor (MSR) is one of the six reactor systems proposed by the Generation IV International Forum [1]. Graphite is used as a neutron moderator and/or structural component in MSR [2–4]. Molten salt as primary coolant flows through graphite moderator channel at high temperature and radiation environment. The fluorine compounds (ClF_3, BrF_3, LiF, etc.) in molten salts can react with graphite [5–8], and the pores in the nuclear graphite can accommodate the molten salt and fission products in normal operation condition [9]. Therefore, it is important to systematically analyze the pore structure characteristics of nuclear graphite in three-dimensional spaces.

IG-110, NBG-18 and NG-CT-10 are nuclear graphite of next-generation nuclear reactors [3, 9–11]. IG-110, which is used in the 10 MW high temperature gas-cooled reactor (HTR-10) in China [12] is quite unique in its variations in the coke type, forming process and heat treatment processes, producing a relatively widespread distribution of initial properties and variation of graphite behavior under irradiation [3]. Recently, microstructures of IG-110, NBG-18 and NG-CT-10 were studied [13–16], and pore structures of virgin nuclear graphite were determined [16].

While 2D analysis is somewhat restricted in terms of directly accessible parameters, 3D analysis is much quicker to examine much larger samples. X-ray micro-computed tomography (μ-CT) is a powerful technique for investigating the pore structure and flow properties such as permeability in 3D spaces. And it is nondestructive for many porous media. Based on 3D images obtained from μ-CT, Berre et al. [4] developed finite-elements models to study microstructure and bulk mechanical properties of Gilsocarbon. It was used to study changes in microstructure of IG-110 nuclear graphite caused by thermal oxidation [17].

In this paper, μ-CT images are used to estimate 3D pore characterization of IG-110, NBG-18 and NG-CT-10, and permeability estimation through geometries is examined.

2 Experimental

2.1 Materials

The nuclear graphite samples include IG-110 (Toyo Tanso Co., Ltd., Japan), NBG-18 (SGL Carbon Group, Germany) and NG-CT-10 (FangDa Carbon New Material Co., Ltd., China). NBG-18 was chosen due to the interest of the Next Generation Nuclear Plant program for high irradiation dose regions of the Very High Temperature Reactor (VHTR). IG-110 is a fine-grained historical reference grade and is being used in VHTR. NG-CT-10 is under development in China in many ways similar to IG-110. Table 1 lists properties of the three types of nuclear graphite. Samples prepared for μ-CT pore analysis were machined into cylinders of Φ 1.5 mm × 10 mm. To prevent oxidation of the graphite, the samples were vacuum dried for 2 h at 150 °C.

2.2 μ-CT and image analysis

The nuclear graphite samples were imaged on a μ-CT at Sanying Precision Engineering Research Center (nanoVoxel-2100, Sanying, China). The system is shown in Fig. 1. An X-rays were generated from a tungsten target bombarded by 60 kV 120 μA electrons and were focused to spot size of 1.5 μm. The sample-to-detector distance was 10 cm and source sample distance was 20 cm. The exposure time was 85 s with pixel size of about 0.91 μm. Since the resolution determines the slice thickness, the minimum voxel size was 0.91 μm × 0.91 μm × 0.91 μm, with voxel values ranging from 0 to 255 corresponding to the attenuation coefficient. A CCD camera was used to obtain two-dimensional X-ray images for 1000 layers. During the CT scan, the sample was rotated at different projection angles between 0° and 180°, in 0.5° steps. The absorption radiographs for different viewing angles were projected onto a CdWO4 fluorescent screen and recorded by the CCD camera of 1024 × 1024 pixel. To correct for electronic noise and variations in the X-ray brightness in the experiment, light-field images (i.e., X-ray illumination on, and the specimen out of the beam) and dark-field images (i.e., X-ray illumination off) were recorded. Projection images were reconstructed using the FDK algorithm developed by Feldkamp [18].

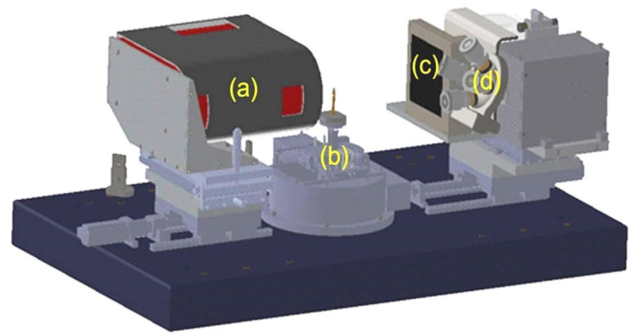

Fig. 1 μ-CT system. *a* X-ray sources system, *b* sample stage, *c* flat panel detector, *d* optocoupler detector system

Image segmentation and pore morphology analysis were completed with the Avizo Fire 8.0 [19]. Sub-volumes of 450 × 450 × 450 voxels (i.e., 410 μm × 410 μm × 410 μm) were extracted from the samples. Before analysis, the IG-110, NGB-18 and NG-CT-10 data were smoothed with non-local means filtering [20] and bilateral filtering, respectively. Then, a locally adaptive segmentation method, such as the indicator kriging method [21], was used to separate pores from the solid phase. Briefly, a lower (T_0) and an upper (T_1) limit were selected by visual inspection of the image histograms. Voxel values below T_0 and above T_1 were identified as the pore and solid phases, respectively. Voxels with grayscale values between T_0 and T_1 were classified as pores or solids depending on the local covariance determination. Details of the indicator kriging method are given in Refs. [21, 22].

2.3 Quantification of 3D microstructures

The workflow to analyze the pore space geometry using Avizo PNM is outlined in Fig. 2. Detailed theories of the processes employed are described in Ref [23]. The medial axis of pore space was extracted from the segmented images and computed using morphological erosion based on the LKC algorithm [24]. The distance between the skeleton and the nearest solid phase was recorded as the burn number. Meanwhile, the medial axis trimming must be performed to remove dead end and isolated paths for the computation of skeletons. Next, pore throats, defined as the

Table 1 Properties of nuclear graphite

Types of nuclear graphite	IG-110	NBG-18	NG-CT-10
Forming method	Isotropic molding	Vibration molding	Isotropic molding
Coke type	Petroleum	Pitch	Petroleum
Average particle size/μm	~20	~300	~25
Porosity/%	20	18.3	24

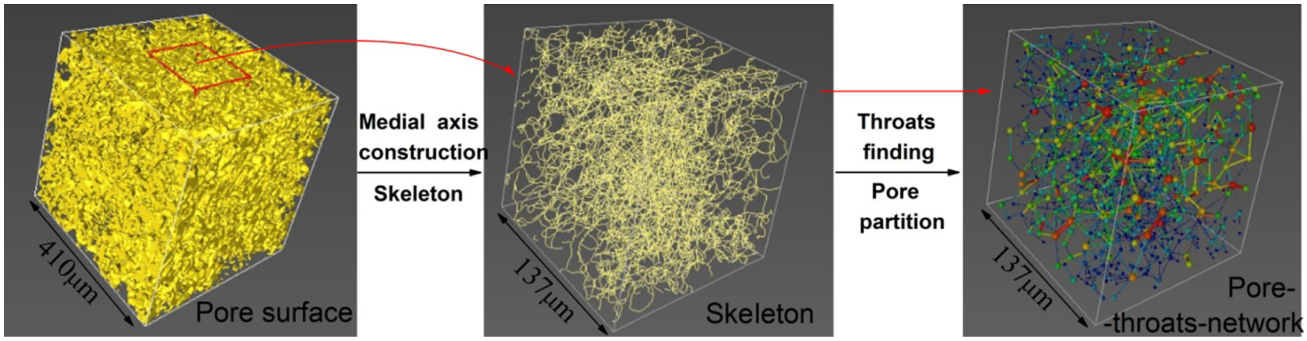

Fig. 2 Schematic sequential diagram of the pore throat network construction

minimum cross-sectional area of each channel, should be found out by Dijkstra shortest paths algorithm [25]. Subsequently, pore and throat structure parameters, such as pore and throat size, surface area, and geometrical tortuosity were analyzed based on pore throat network and the medial axis.

2.4 Permeability simulation and estimation

The absolute permeability was simulated using Avizo Xlab-Hydro (Fig. 3) with input of the modified binary images. Stokes equation [26] was solve based on a finite-volume method which builds the volume mesh

$$\nabla\mu = 0; \quad \nabla P = \mu\nabla^2 u \tag{1}$$

where u is the fluid velocity vector, P is the pressure, and μ is the dynamic viscosity. The absolute permeability [27] was evaluated by Darcy's law. And the Avizo Xlab-Hydro solver was validated by comparing with theoretical models and standard glass bead packaging models [28].

$$O/S = -k\nabla P/(\mu L) \tag{2}$$

where O/S is Darcy's velocity, k is the absolute permeability, μ is the dynamic viscosity of the flowing fluid, ∇P is the pressure difference applied around the sample, and L is the length of the sample in the flow direction.

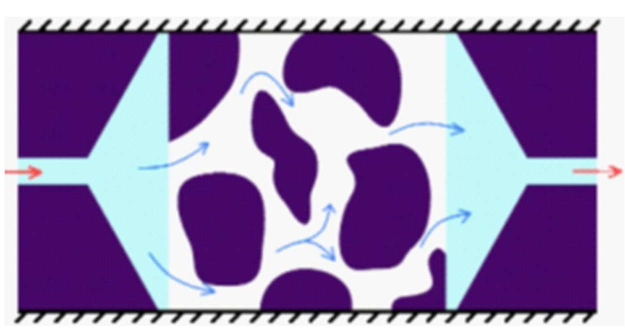

Fig. 3 Typical computational geometries used for Avizo simulations

3 Results and discussion

3.1 Slice analysis for the nuclear graphite samples

The μ-CT is an effective tool for visualization of an arbitrary cross section (slice) in the samples. It is possible to analyze the morphological characteristics on any slice without damaging the nuclear graphite samples. The SEM images and the tomographic images after μ-CT recovery data are shown in Fig. 4. The shrinkage cracks formed during calcinations, and pore structure, can be seen in the images. However, they are of different types. In Fig. 4a and b, the shrinkage cracks run parallel to the major axis of the particle in IG-110. Figure 4d and e shows that NG-CT-10 has similar microstructure to IG-110, but the pores in NG-CT-10 are more elliptical, and shrinkage cracks are more numerous and of greater thickness, than those observed in IG-110. The filler material in NBG-18, pitch-based graphite, appears to be spherical in nature, but the shrinkage cracks in NBG-18 vary greatly in size. Many larger shrinkage cracks, as shown in Fig. 4g and h, are oriented with their long axis approximately tangential to the particle's radial direction. While the IG-110 and NG-CT-10 samples have small pores, the NBG-18 has much bigger pore inside. This is consistent with the SEM results in Ref [9].

Figure 4 shows that NBG-18 has more big pores than IG-110 and NG-CT-10. This may lead to greater molten salt infiltrate. The 3D pore structures for IG-110 and NG-CT-10 exhibit similar honeycomb patterns, while continuous longer and bigger channels were found in the NBG-18 only. It is good for gas diffusion and molten salt flowing.

3.2 Quantification of pore and throat networks

The reconstructed 3D model of pore structure and the pore throat network for the three types of nuclear graphite are shown in Fig. 5. Their general pore and throat structure information are given in Table 2.

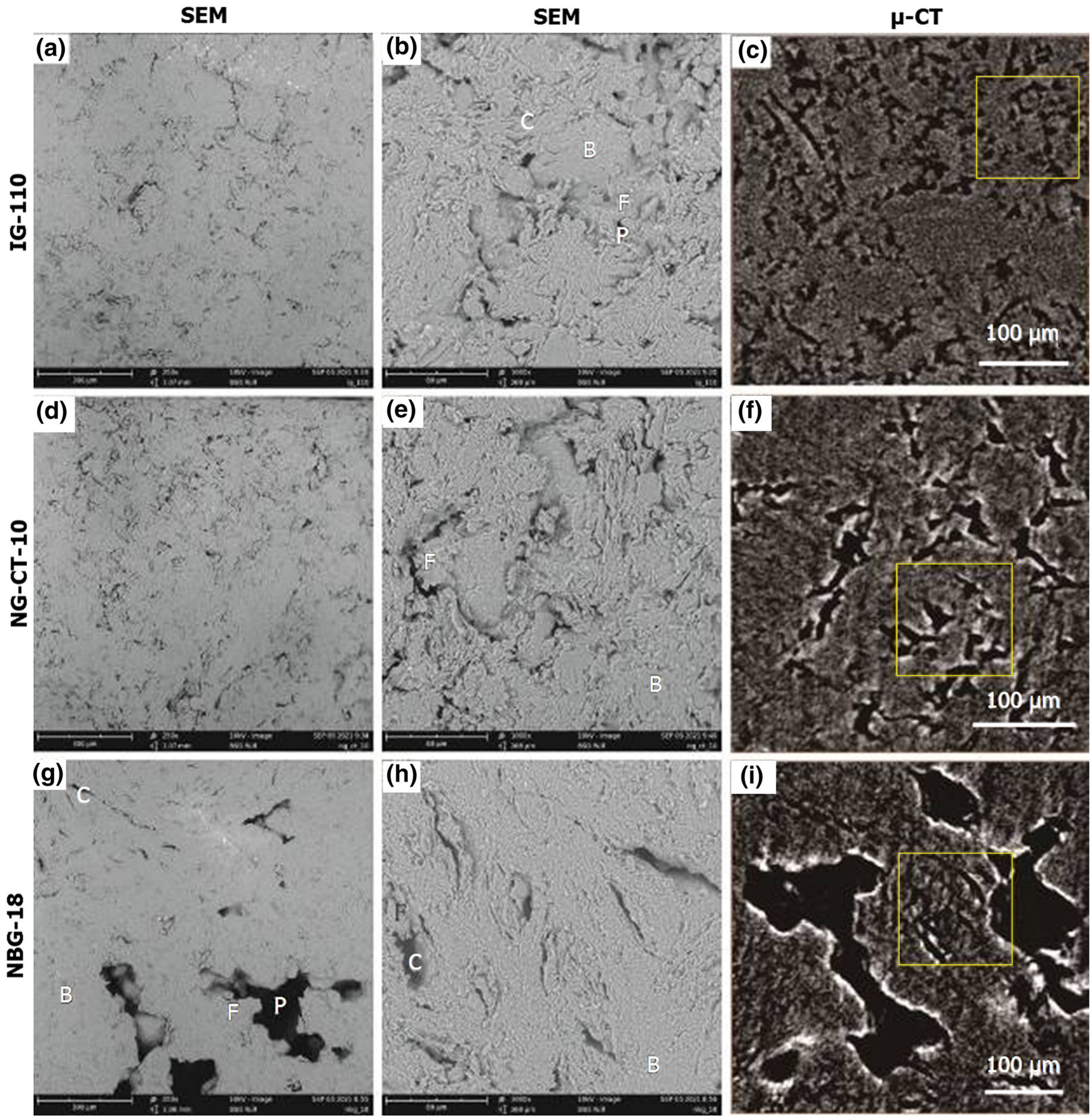

Fig. 4 SEM images and CT images of IG-110, NG-CT-10 and NBG-18. *P* pore, *B* binder, *F* filler, *C* shrinkage crack

The rainbow colors nodal in Fig. 5b represent the pore diameter, and the distance of two pores represents the throat structure. The porosity is 27.1 % for IG-110 and 28.9 % for NG-CT-10, being slightly higher than the data in Ref [12]. The μ-CT can detect the close pore in nuclear graphite, which may cause slightly increase in porosity. The porosity of NBG-18 is as big as 50.1 %, because of much bigger pores in this type of graphite. Therefore, it would provide much more spaces for molten salts. As known, more pathways can lead to a more connected pore network and less tortuous pathway through the volume. The pore connectivity rates are 97.6 %, 99.8 % and 98.6 % for IG-110, NG-CT-10 and NBG-18, respectively. This is much convenient for gas diffusion and molten salt flowing.

From Table 2, NBG-18 has the highest porosity and the most pores and throats, and the biggest mean area of throats and average coordination number. The bigger pores

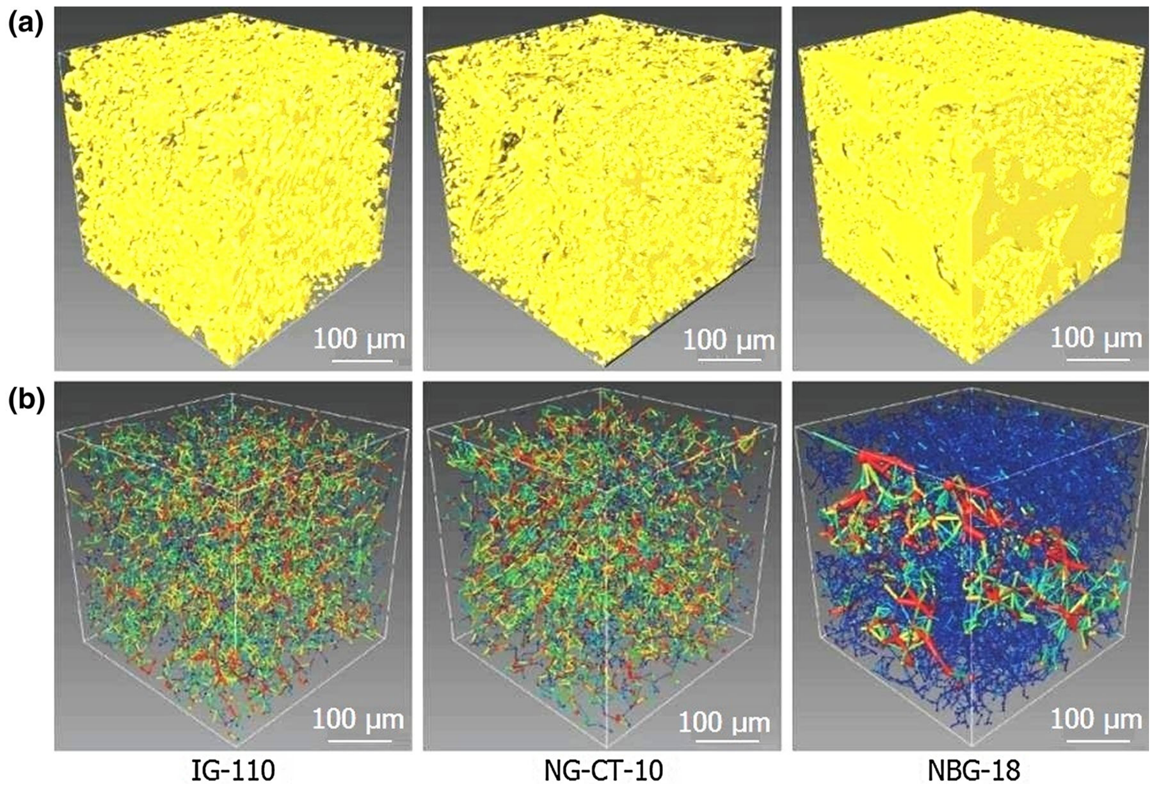

Fig. 5 3D structure (**a**) and pore throat networks (**b**) of IG-110, NG-CT-10 and NBG-18 nuclear graphite samples (410 μm × 410 μm × 410 μm). The *rainbow colors* represent distance of the path to the closest grain voxels, with *blue color* being very narrow channels, and *red color* being wider channels. (Color figure online)

Table 2 Properties of the graphite microstructure

Pore properties	IG-110	NG-CT-10	NBG-18
Porosity/%	27.11	28.94	50.09
Connectivity rate of pores/%	97.61	99.78	98.62
Total number of pores	17,613	21,306	30,401
Total number of throats	35,862	45,932	102,585
Mean area of throats/μm^2	19.21	18.66	20.15
Average length of throats/μm	13.66	13.22	12.74
Average coordination number	4.07	4.31	6.75
Tortuosity of throats channel	1.66	1.71	1.37

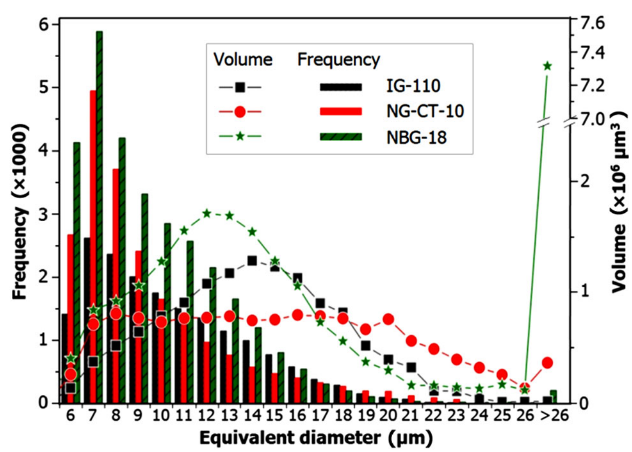

Fig. 6 Pore size–volume distribution for IG-110, NG-CT-10 and NBG-18

formed by vibration can have a major effect on water or molten salt flow.

Pore size distribution is expressed as the frequency distribution of logarithmic effective radii. As shown in Fig. 6, pore sizes of the three types of nuclear graphite are in unimodal structure peaked at around 7 μm of equivalent diameter. The pore size volumes are peaked at 14 and 12 μm for IG-110 and NBG-18, respectively, but the pore size volume of NG-CT-10 is almost the same at equivalent diameters of 4–20 μm.

The coordination number of nodal pore in nuclear graphite is the number of its near neighbors. The average coordination numbers are 4.07, 4.31 and 6.75 for IG-110, NG-CT-10 and NBG-18, respectively. Figure 7a shows the distribution of coordination number of the nuclear graphite samples. The NBG-18 differs greatly from IG-110 and NG-CT-10 in coordination number distribution. Meanwhile, the most irregular paths, with coordination number values

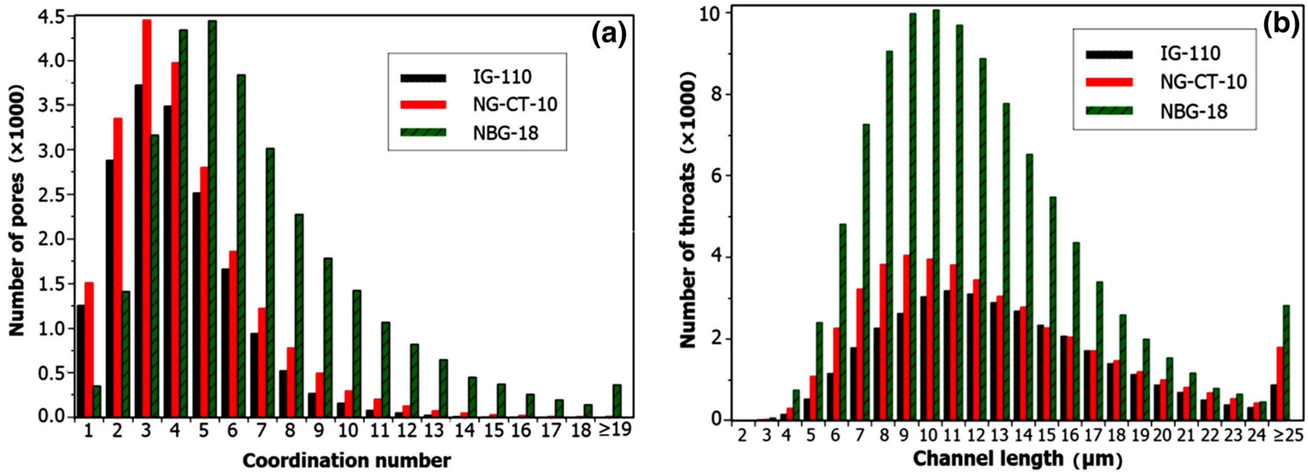

Fig. 7 Pore coordination number distribution (**a**) and channel length distribution (**b**) for IG-110, NG-CT-10 and NBG-18

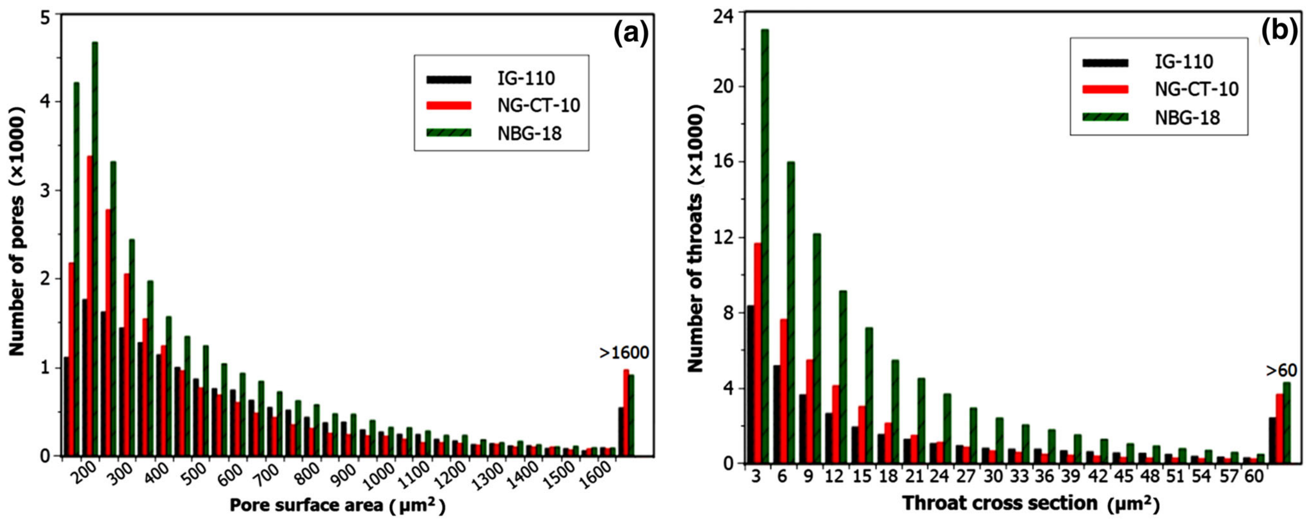

Fig. 8 Pore surface area (**a**) and throats cross section distribution (**b**) for IG-110, NG-CT-10 and NBG-18

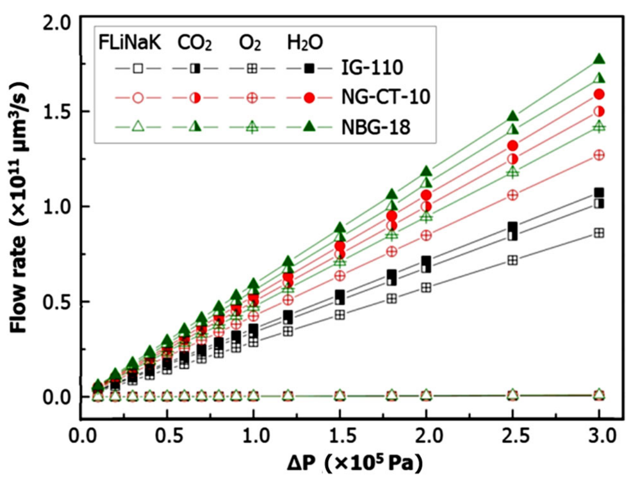

Fig. 9 Volume flow rate versus applied pressure gradient. The linear relationship validates the Darcy's law

larger than 15, were observed in the NBG-18 sample. This might be due to the larger pore size and better connectivity. More coordination numbers can lead to more connected pore networks. The coordination number of the three types of nuclear graphite are well distributed, hence desirable interconnect pore networks for gas diffusion and molten salt flowing.

Throat channel length refers to the distance between the centers of two adjacent nodal pores. This distance was measured along the medial axis rather than along the straight line between the two centers. The throat channel length distributions are shown in Fig. 7b. The channel length ranges are 3–45, 3–59 and 3–104 μm for IG-110, NG-CT-10 and NBG-18, respectively. While the NBG-18 has the widest throat channel length range, the average throat lengths of IG-110 (13.7 μm) and NG-CT-10 (13.2 μm) are slightly greater than NBG-18 (12.7 μm).

In addition to pore size, pores coordination numbers and throat channel length, the interaction between the nuclear graphite and molten salt/oxygen was closely influenced by the pore surface area and the cross section of throats. The pore surface areas for IG-110, NG-CT-10 and NBG-18 ranged 103–4347, 103–8270, and 103–60805 μm^2, respectively. Their distributions are shown in Fig. 8a, peaked at around 200 μm^2 for all the three types of nuclear graphite. The NBG-18 has the largest number of pores and throats. Figure 8b shows that throat cross sections of the three samples are of similar distribution. Of the three types of nuclear graphite, NBG-18 has the largest pore surface area and throat cross section, i.e., the most vulnerable to damages by molten salt/oxygen. Yang et al. [29] indicated that the C-F bond could be formed in the IG-110 samples soaking with molten fluoride salts at 650 °C. So the surface area and throat cross section may play an important role in graphite infiltration experiment, which requires further study in future.

These results, together with the 2D and 3D observation, indicate that NBG-18 differs greatly in structure from IG-110 and NG-CT-10, and the IG-110 and NG-CT-10 may be more suitable for use in molten salt reactor.

3.3 The absolute permeability in pore throat network of three nuclear graphite samples

Numerical analysis of a single-phase flow (H_2O, CO_2, O_2, FLiNaK) through a porous medium was performed. In order to validate the mathematical model, a parametric study was performed by varying the pressure gradient across the porous structure and calculating the corresponding flow rates. The flow rate varied linearly with the applied pressure gradient, as shown in Fig. 9. This indicates that the Darcy's law for the present computational geometry can be applied to the porous structure. The absolute permeability of NBG-18 (0.106 mD) is much higher than IG-110 (0.064 mD) and NG-CT-10(0.090 mD).

For the porous material, according to the realistic porous geometry of pore structure by μ-CT to make a numerical simulation analysis is an effective method. This study indicates that the NBG-18 has a large number of pores and high connectivity, so the molten salt may easily infiltrate graphite, while the IG-110 and NG-CT-10, having uniformly distributed small pores, are more suitable for use in molten salt reactor.

4 Conclusion

Nuclear graphite samples of IG-110, NG-CT-10 and NBG-18 were characterized by X-ray tomography method. Microstructure of the pore size distribution and key shape parameters (i.e., throat area, throat channel length, and throat channel tortuosity) were determined. This provides convenience for future research on graphite infiltration experiment. The IG-110 and NG-CT-10, with a similar microstructure, differ greatly from NBG-18. The absolute permeability of IG-110, NG-CT-10 and NBG-18 were investigated within the pore structure of realistic porous geometry derived μ-CT, which is an easy and effective tool for study on molten salt flowing.

References

1. A Technology Roadmap for Generation IV Nuclear Energy Systems, US DOE Nuclear Energy Research Advisory Committee and the Generation IV International Forum, December 2002, GIF-002-00
2. W. Windes, T. Burchell, R. Bratton. Report—INL/EXT-07-13165, 2007
3. R. Bratton, W. Windes. Report—ORNL/TM-2007/153-10-07 2010
4. C. Berre, S.L. Fok, P.M. Mummery et al., Failure analysis of the effects of porosity in thermally oxidised nuclear graphite using finite element modelling. J. Nucl. Mater. **381**, 1–8 (2008). doi:10.1016/j.jnucmat.2008.07.021
5. A.S. Nazarov, V.G. Makotchenko, V.E. Fedorov, Preparation of low-temperature graphite fluorides through decomposition of fluorinated-graphite intercalation compounds. Inorg. Mater. **42**, 1260–1264 (2006). doi:10.1134/S002016850611015x
6. J. Giraudet, M. Dubois, K. Guerin et al., Solid-state NMR study of the post-fluorination of (C2.5F)n fluorine-GIC. J. Phys. Chem. B **111**, 14143–14151 (2007). doi:10.1021/Jp076170g
7. M. Dubois, K. Guerin, J.P. Pinheiro et al., NMR and EPR studies of room temperature highly fluorinated graphite heat-treated under fluorine atmosphere. Carbon **42**, 1931–1940 (2004). doi:10.1016/j.carbon.2004.03.025
8. X.M. Yang, S.L. Feng, X.T. Zhou et al., Interaction between nuclear graphite and molten fluoride salts: A synchrotron radiation study of the substitution of graphitic hydrogen by fluoride ion. J. Phys. Chem. A **116**, 985–989 (2012). doi:10.1021/Jp208990y
9. G.Q. Zheng, P. Xu, K. Sridharan et al., Characterization of structural defects in nuclear graphite IG-110 and NBG-18. J. Nucl. Mater. **446**, 193–199 (2014). doi:10.1016/j.jnucmat.2013.12.013
10. L. Hongwei, G. Mingshan, S. Libin. Strength Weibull distribution analysis for the NBG-18 graphite in HTR. Trans. SMiRT **19**, 2025–2082 (2007)
11. T.R. Allen, K. Sridharan, L. Tan et al., Materials challenges for generation IV nuclear energy systems. Nucl. Technol. **162**, 342–357 (2008)
12. J. Sumita, T. Shibata, I. Fujita et al., Development of evaluation method with X-ray tomography for material property of IG-430 graphite for VHTR/HTGR. Nucl. Eng. Des. **271**, 314–317 (2014). doi:10.1016/j.nucengdes.2013.11.053
13. C. Karthik, J. Kane, D.P. Butt et al., Microstructural characterization of next generation nuclear graphites. Microsc. Microanal. **18**, 272–278 (2012). doi:10.1017/S1431927611012360
14. C. Karthik, J. Kane, D.P. Butt et al., In situ transmission electron microscopy of electron-beam induced damage process in nuclear grade graphite. J. Nucl. Mater. **412**, 321–326 (2011). doi:10.1016/j.jnucmat.2011.03.024

15. R.K.L. Su, H.H. Chen, S.L. Fok et al., Determination of the tension softening curve of nuclear graphites using the incremental displacement collocation method. Carbon **57**, 65–78 (2013). doi:10.1016/j.carbon.2013.01.033
16. J. Kane, C. Karthik, D.P. Butt et al., Microstructural characterization and pore structure analysis of nuclear graphite. J. Nucl. Mater. **415**, 189–197 (2011). doi:10.1016/j.jnucmat.2011.05.053
17. J. Sumita, T. Shibata, E. Kunimoto et al., The development of a microstructural model to evaluate the irradiation-induced property changes in IG-110 graphite using x-ray tomography. R. Soc. Chem. **328**, 163–170 (2010)
18. L.A. Feldkamp, L.C. Davis, J.W. Kress, Practical cone-beam algorithm. J. Opt. Soc. Am. A **1**, 612–619 (1984). doi:10.1364/Josaa.1.000612
19. H. Wang, L.J. Ma, K.C. Cao et al., Selective solid-phase extraction of uranium by salicylideneimine-functionalized hydrothermal carbon. J. Hazard. Mater. **229**, 321–330 (2012). doi:10.1016/j.jhazmat.2012.06.004
20. A. Buades, B. Coll, V. Morel, A non-local algorithm for image denoising. Proc. CVPR IEEE **2**, 60–65 (2005). doi:10.1109/CVPR.2005.38
21. W. Oh, W.B. Lindquist, Image thresholding by indicator kriging. IEEE Trans Pattern Anal **21**, 590–602 (1999). doi:10.1109/34.777370
22. S. Peth, R. Horn, F. Beckmann et al., Three-dimensional quantification of intra-aggregate pore-space features using synchrotron-radiation-based microtomography. Soil Sci. Soc. Am. J. **72**, 897–907 (2008). doi:10.2136/sssaj2007.0130
23. W.B. Lindquist, A. Venkatarangan, Investigating 3D geometry of porous media from high resolution images. Phys. Chem. Earth Part A **24**, 593–599 (1999). doi:10.1016/S1464-1895(99)00085-X
24. T.C. Lee, R.L. Kashyap, C.N. Chu, Building skeleton models via 3-D medial surface axis thinning algorithms. CVGIP-Graph Model Image Process. **56**, 462–478 (1994). doi:10.1006/cgip.1994.1042
25. W.B. Lindquist, A. Venkatarangan, J. Dunsmuir et al., Pore and throat size distributions measured from synchrotron X-ray tomographic images of Fontainebleau sandstones. J. Geophys. Res. **105**, 21509–21527 (2000). doi:10.1029/2000jb900208
26. B.J. Zhu, H.H. Cheng, Y.C. Qiao et al., Porosity and permeability evolution and evaluation in anisotropic porosity multiscale-multiphase-multicomponent structure. Chin. Sci. Bull. **57**, 320–327 (2012). doi:10.1007/s11434-011-4874-4
27. J.M. Sharp, C.T. Simmons, The compleat Darcy: new lessons learned from the first English translation of Les Fontaines publiques de la Ville de Dijon. Ground Water **43**, 457–460 (2005). doi:10.1111/j.1745-6584.2005.0076.x
28. S. Peng, F. Marone, S. Dultz, Resolution effect in X-ray microcomputed tomography imaging and small pore's contribution to permeability for a Berea sandstone. J. Hydrol. **510**, 403–411 (2014). doi:10.1016/j.jhydrol.2013.12.028
29. X. Yang, S. Feng, X. Zhou et al., Interaction between nuclear graphite and molten fluoride salts: a synchrotron radiation study of the substitution of graphitic hydrogen by fluoride ion. J. Phys. Chem. A **116**, 985–989 (2012). doi:10.1021/jp208990y